communications chemistry

A Nature Portfolio journal

Article

https://doi.org/10.1038/s42004-025-01704-x

Determining structure and Zn-specific Lewis acid-base descriptors for diorganozincs in non-coordinating solvents using X-ray spectroscopy

Lewis G. Parker[1], Frances K. Towers Tompkins[1], Jake M. Seymour[1], Najaat Alblewi[1], Ekaterina Gousseva[1], Megan R. Daw[1], Shusaku Hayama[2], Richard P. Matthews[3], Adam E. A. Fouda[4,5], Joshua D. Elliott[2], Christopher D. Smith[1] ✉ & Kevin R. J. Lovelock[1] ✉

Diorganozinc reagents (ZnR_2, e.g. R = Et, Ph, C_6F_5) are widely used as Lewis acid catalysts or Lewis base reagents in their own right. However, descriptors for predicting the influence of the R substituent on ZnR_2 Lewis acidity/basicity are very sparse. This is because ZnR_2 liquid-phase speciation and electronic structure are unknown to date due to zinc's '*spectroscopically quiet*' nature and inability to measure '*at zinc*'. Here, we identify the geometric structures of ZnR_2 in weakly coordinating solvents, demonstrating that electronic structure factors will dominate reactivity. We quantify the electronic structure properties that dictate ZnR_2 Lewis acidity/basicity using three newly developed zinc-specific descriptors by combining the results from three zinc-specific X-ray spectroscopy methods and calculations. We provide accessible methods to pre-screen ZnR_2 reactivity. Furthermore, our X-ray spectroscopy toolkit offers opportunities to develop liquid-phase descriptors that dictate reactivity for other zinc species, e.g. zinc bis-amides, battery electrolytes and enzymes.

Diorganozincs (ZnR_2)[1,2] have a special place in chemical history; diethylzinc ($ZnEt_2$) was amongst the first organometallics (Frankland C19th)[3]. ZnR_2 can range in reactivity from Lewis basic/nucleophilic (*i.e.* electron donating) in e.g. transmetalation[4] or nucleophilic substitution reactions[5–12] through to Lewis acidic/electrophilic[9,11–20] (*i.e.* electron acceptor). This diversity of reactivity has led to considerable liquid-phase applications in synthetic chemistry: the Nobel Prize-recognised Negishi cross-coupling reaction[21–25]; asymmetric autocatalysis of the Soai reaction[26]; Lewis acid catalysis[27]; frustrated Lewis pair catalysts (FLPs)[15]; insertion chemistries (CO_2 and SO_2)[28,29]; transfer reagents[30–33]; and in nanomaterial preparation[13,14].

These significant advances in ZnR_2 chemistry have been driven mainly by empirical, iterative synthetic experimentation, as liquid-phase ZnR_2 species are *spectroscopically quiet* (Fig. 1)[34,35]. In a telling approach, the enzymatic community at times have substituted Zn^{2+} for other metal cations (e.g. Co^{2+}, Cu^{2+}, Cd^{2+} etc.) that were easier to observe spectroscopically in model systems[34]. This spectroscopic near-silence has led to a dearth of descriptors for ZnR_2, severely limiting the interpretation, prediction and fine-tuning of ZnR_2 reactivity. Liquid-phase EPR and UV-Vis spectroscopies are ineffective for producing descriptors for closed-shell d^{10} Zn^{2+}. One quantitative Lewis acidity descriptor, the electron acceptor number measured using ^{31}P NMR spectroscopy, has been used for three ZnR_2 compounds[11]. This method investigates the interaction of ZnR_2 with triethylphosphine oxide. However, it is unsatisfactory because the phosphorus atom is positioned at a distance from the zinc centre[36], which is the site of ZnR_2 reactivity e.g. electron acceptance for Lewis acidic ZnR_2.

Experimental or calculated electronic structure data is often used to produce Lewis basicity/acidity descriptors[37–40]. Advantageously, these intrinsic descriptors capture Lewis basicity/acidity independent of any probe molecule. However, liquid-phase experimental electronic structure spectroscopy has been severely limited by experimental challenges. Due to the vacuum conditions required, liquid-phase photoelectron spectroscopy studies are very challenging even for simple aqueous solutions[41], let alone very reactive ZnR_2 solutions. Gas-phase photoelectron spectroscopy has been used to produce a Lewis basicity descriptor, the highest occupied molecular orbital (HOMO) energy, for four ZnR_2 (R = alkyl)[38]; however, this descriptor is not representative of liquid-phase ZnR_2, leaving a huge

[1]Department of Chemistry, University of Reading, Reading, UK. [2]Diamond Light Source, Harwell Science and Innovation Campus, Didcot, UK. [3]Department of Biosciences, University of East London, London, UK. [4]Department of Physics, The University of Chicago, Chicago, IL, USA. [5]Chemical Sciences and Engineering Division, Argonne National Laboratory, Lemont, IL, USA. ✉e-mail: c.d.smith@reading.ac.uk; k.r.j.lovelock@reading.ac.uk

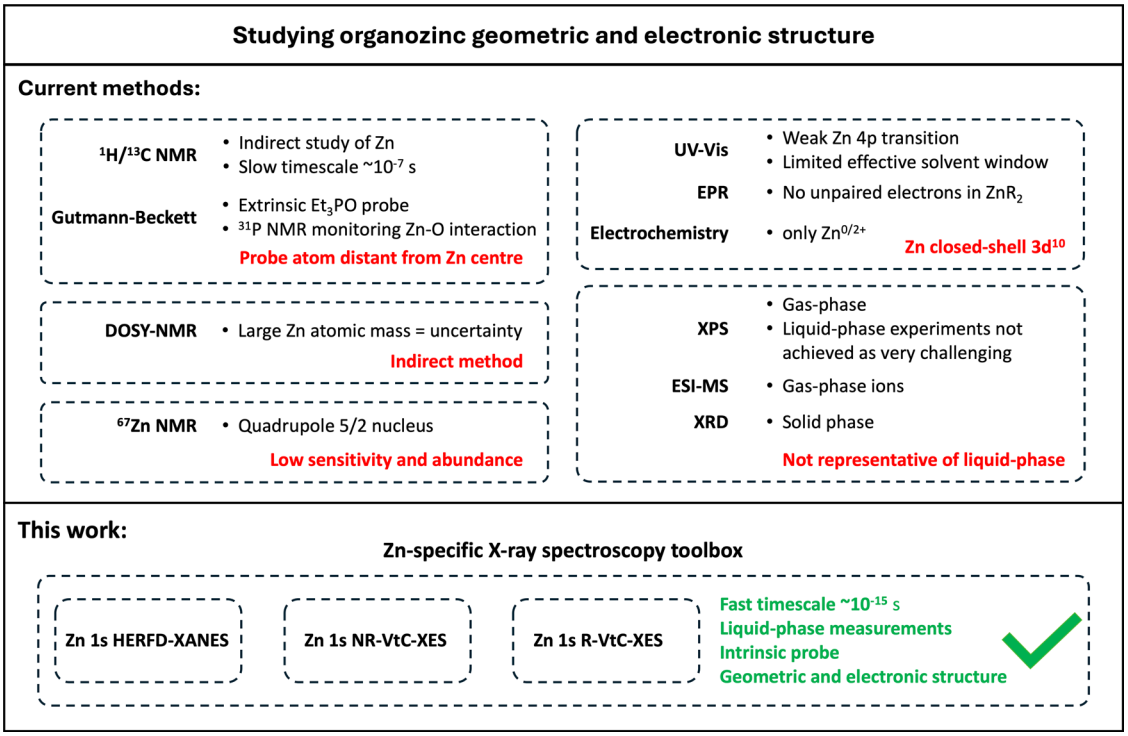

Fig. 1 | Current diorganozinc analysis methods, their limitations, and our liquid-phase X-ray spectroscopy approach. Overview of current methods for studying ZnR_2 complexes and their shortcomings and our work here using an advanced X-ray spectroscopy toolkit for studying liquid-phase ZnR_2 complexes.

unanswered question over solvent influence. Therefore, for liquid-phase ZnR_2 the frontier orbitals (e.g. the HOMO and the lowest unoccupied molecular orbital, LUMO) have never been experimentally investigated let alone quantified.

In this article we use zinc-specific X-ray spectroscopies to produce zinc-specific, intrinsic descriptors, as hard X-ray spectroscopies overcome experimental challenges for liquid-phase studies as vacuum conditions are not required[42,43]. The zinc-specificity of these X-ray spectroscopy-derived descriptors give direct insight into the zinc centre, where ZnR_2 reactivity occurs, e.g. electron donation for Lewis basic/nucleophilic ZnR_2. Zn 1s X-ray absorption near edge structure (XANES) spectroscopy has been used widely for liquid-phase zinc compounds but sparingly for organozinc compounds[44–46]. Only two liquid-phase studies of Zn 1s non-resonant valence-to-core X-ray emission spectroscopy (NR-VtC-XES) are known, both for $ZnCl_2$-based samples[47,48], and none for Zn 1s resonant VtC-XES (R-VtC-XES), highlighting the novelty of our approach. For metals, the main usage of XANES, NR-VtC-XES and R-VtC-XES has been fourth period (i.e. first row) transition metals[42,43,49–52].

In part one of our article, we determine *speciation and geometric structure* for 14 ZnR_2 using a combination of synchrotron-based Zn 1s high-energy-resolution fluorescence detected (HERFD)-XANES spectroscopy (Fig. 2a), density functional theory (DFT) and time-dependent DFT (TDDFT) calculations. To produce intrinsic descriptors, the structure of ZnR_2 must be known, so the influence on reactivity of steric factors relative to electronic structure factors can be considered. Synthetic chemists are in the very unusual position where the starting geometric structures of ZnR_2 in toluene/hexane[9–12] are poorly understood; indeed, the geometric structures of ZnR_2 "*reagents in non-coordinating solvents remain scattered and elusive*"[53]. The ^{67}Zn nucleus (spin 5/2) possesses low NMR sensitivity and gives very broad features so geometric structural conclusions cannot be drawn. Other NMR active nuclei (e.g. ^{1}H and ^{13}C) are distant from the reactive Zn centre and, coupled with the nature of NMR (through-bond and through-space effects), makes relating chemical shift with geometric structure unreliable. Linearity (i.e. C-Zn-C angle of 180°) has been inferred for some ZnR_2 using indirect methods, e.g. melting points, boiling points, solubility, and dipole moment determination[54,55]. In contrast, diffusion-ordered spectroscopy (DOSY) NMR studies in [D_8]toluene suggested that $ZnPh_2$ can form dinuclear $(ZnPh_2)_2$[9], although the relatively high atomic weight of zinc and elongated shape of $ZnPh_2$ make this interpretation very uncertain[9,56,57]. Furthermore, in the solid-phase, $ZnPh_2$ displayed dinuclear three-coordinate bridging $(ZnPh_2)_2$[54]. XANES spectroscopy showed that $ZnEt_2$ is linear in toluene (i.e. C-Zn-C angle of 180°), but no other R substituents were studied[45].

In part two of our article, we use a combination of NR-VtC-XES (Fig. 2b) and Zn 1s HERFD-XANES spectroscopy (Fig. 2a) to identify the zinc-containing occupied molecular orbitals (OMOs) and unoccupied molecular orbitals (UMOs). This identification is essential for producing zinc-specific descriptors, and also allows us to highlight the OMOs and UMOs that give ZnR_2 their remarkable reactivity compared to other common zinc-containing species such as $[Zn(OH_2)_6]^{2+}$ and $ZnCl_2(THF)_2$.

In part three of our article, we describe a *new approach* using zinc-specific X-ray spectroscopy experiments and calculations to produce three zinc-specific (*i.e.* local), intrinsic[36] descriptors: zinc-specific *hardness* (η_{Zn}), zinc-specific *absolute electronegativity* (χ_{Zn}, the negative of the zinc-specific electronic chemical potential, μ_{Zn}) and zinc-specific global electrophilicity index (ω_{Zn}). To obtain η_{Zn}, χ_{Zn} and ω_{Zn}, we combine our knowledge on experimental R-VtC-XES (Fig. 2c), zinc-containing OMOs and UMOs, and DFT calculations (underpinned by the theories of Pearson[37,39,40]).

Results and discussion

Speciation and geometry

All ZnR_2 compounds (typically 0.1 M) in toluene studied here have a *linear* C-Zn-C structure, *i.e.* a C-Zn-C angle of 180°. The Zn 1s HERFD-XANES spectra for all ZnR_2 in toluene (Figs. 3a, 4a and Supplementary Fig. 1) and $ZnEt_2$ in hexane (Supplementary Fig. 2) gave a single sharp, intense peak at a low incident energy of ~9661 eV. This common motif for linear two-coordinate complexes, e.g. copper complexes[58], has previously been observed for $ZnEt_2$ in toluene using standard resolution XANES spectroscopy[45], and is due to two absorption transitions; Zn 1s to two degenerate UMOs with very strong Zn p contributions (discussed further

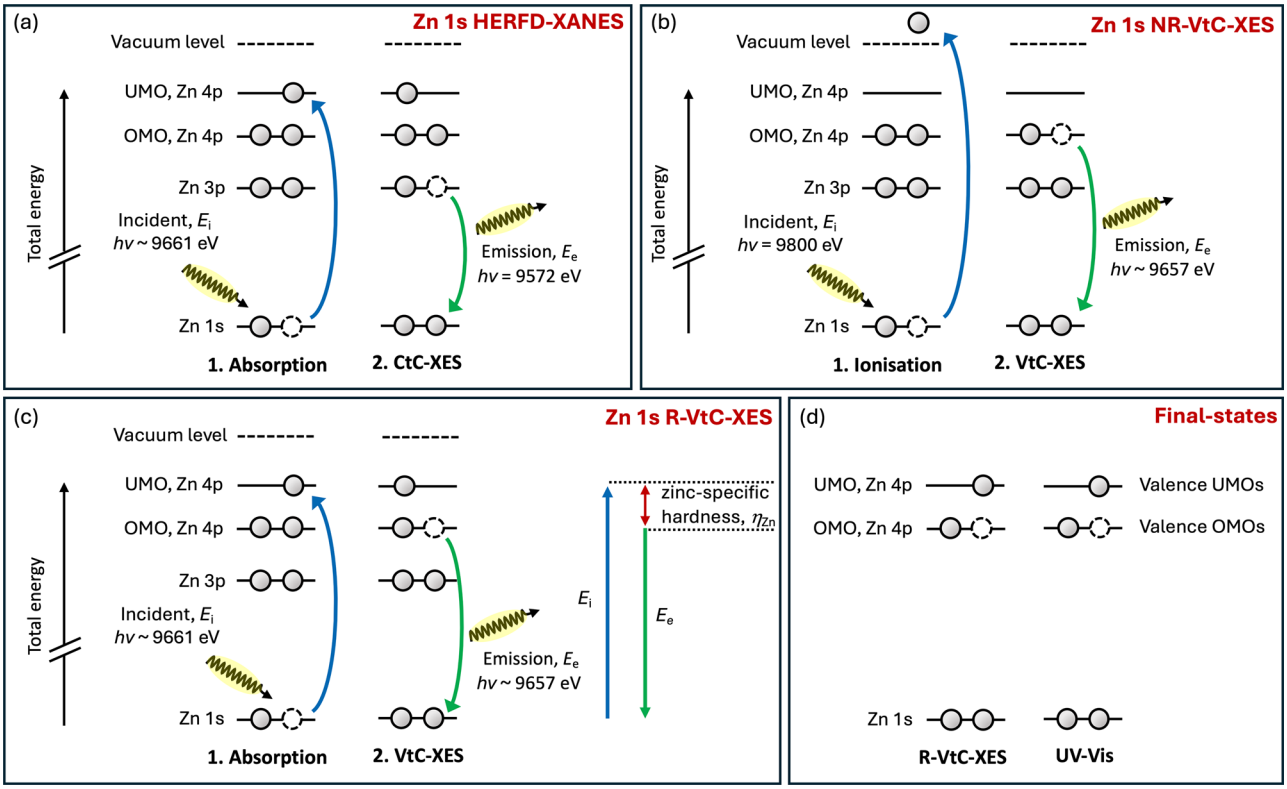

Fig. 2 | Probing electronic transitions in diorganozinc complexes. A new spectroscopic approach for ZnR_2. Electronic transition schematic of ZnR_2 complexes studied: **a** Zn 1s HERFD-XANES, **b** Zn 1s NR-VtC-XES, **c** Zn 1s R-VtC-XES, **d** final-states of Zn 1s R-VtC-XES and UV-Vis spectroscopy.

below). In contrast to linear ZnR_2, the Zn 1s HERFD-XANES spectra for octahedral $[Zn(NCMe)_6]^{2+}$ and $[Zn(OH_2)_6]^{2+}$ and tetrahedral $ZnCl_2(THF)_2$ gave broader, lower intensity peaks at higher incident absorption energy (Fig. 3a). The excellent visual match of experimental Zn 1s HERFD-XANES spectra (Figs. 3a, 4a) and calculated XANES spectra (Figs. 3b, 4b), give high confidence that we have captured the speciation and geometric structure correctly in our calculations. These linear structures in relatively non-coordinating solvents are analogous to gas- and solid-state linear structures for ZnR_2, i.e. in the absence of any solvent molecules[38,59].

There is the potential for liquid-phase flex in the C-Zn-C linear bonds for ZnR_2 away from a C-Zn-C angle of 180°. Using calculated total energies for $ZnEt_2$, the structure at 180° is the most stable; decreasing the C-Zn-C angle decreases the structure stability (Supplementary Table 1 and Supplementary Fig. 3). However, when the C-Zn-C angle is greater than 160° the calculated XANES spectra are very similar to that for the structure with C-Zn-C angle at 180° (Supplementary Fig. 3); our experimental data cannot distinguish between structures with a C-Zn-C angle of between 180° and 160°. Furthermore, the calculated total energies for structures with a C-Zn-C angle greater than 160° are within 10 kJ mol^{-1}; therefore, whilst the structure at C-Zn-C angle of 180° is the most stable, we cannot rule out slight flexing of the C-Zn-C angle away from 180° (i.e. linear) in the liquid-phase. The dihedral angles (eclipsed 0° or staggered 90°) between the two R substituents gave, within calculated uncertainty, the same total energies (Supplementary Figs. 4,5 and Supplementary Table 2–4). Therefore, both conformers are very likely to be present in the solution for ZnR_2.

No evidence for the existence of bimetallic bridging structures was found. The calculated XANES spectrum for dimeric $(ZnPh_2)_2$, based on a solid-state structure[54], shows a clear loss of the sharp, intense peak at low incident energy (Supplementary Fig. 6). This is as expected for a three-coordinate, non-linear zinc centre, as the UMO degeneracy is lifted compared to two-coordinate linear $ZnPh_2$[58]. Furthermore, all ZnR_2 compounds studied here gave very similar experimental and calculated Zn 1s HERFD-XANES spectra with relatively sharp absorption features at low incident energy, showing that bridging species were not present in significant concentration.

Electronic-structure-based descriptors will explain the reactivity of two-coordinate, linear ZnR_2 because the zinc centre is sterically accessible. The vdW space filling structures for ZnR_2 studied here, even $Zn(C_6F_5)_2$ and $Zn(t\text{-}Bu)_2$ with their relatively bulky ligands, all have a clearly visible zinc centre (Figs. 3, 4, right-hand side, Supplementary Fig. 7). In contrast, for the four- and six-coordinate species, the zinc centre is shielded by the ligands and is not visible in the vdW space filling structures (Fig. 3, right-hand side). Therefore, steric hindrance by the R substituents on ZnR_2 is unlikely to be a factor in deciding reactivity at the zinc, especially when the zinc centre is acting as an electron acceptor. Furthermore, all ZnR_2 in non-coordinating solvents are coordinatively unsaturated. Hence, all ZnR_2 can form a bond to an electron donor ligand without the need to first break a Zn-ligand bond, e.g. $ZnMe_2 + THF$ to form $ZnMe_2(THF)_2$[60]. Furthermore, binding of a chiral Lewis donor substrate/ligand to the coordinatively unsaturated zinc centre has been shown to allow a range of stereoselective reactions to be performed[26,61].

Molecular orbital identification—Why are ZnR_2 so remarkable?

Given the importance of the sterically accessible zinc centre in all ZnR_2, it is vital to build a picture of the frontier molecular orbitals with significant zinc contributions, as these MOs will control reactivity instead of stereochemical factors. We will demonstrate why the remarkable reactivity of ZnR_2 occurs relative to other common zinc-containing species.

For all ZnR_2 where R = alkyl the only MO with a significant Zn p contribution (~ 16% Zn p, Supplementary Table 5) is the HOMO (Fig. 4f and Supplementary Figs. 9–14). This is a remarkable result given that the formal oxidation state is Zn^{2+}, with the expectation being that electron density of frontier OMOs would reside mainly on the ligands. For R = aryl the OMO,Zn p is the HOMO-4 (with the HOMO to HOMO-3 from the aryl substituents, Fig. 4f, Supplementary Table 5 and Supplementary Figs. 15–24). These identifications are based on the intense, narrow, high

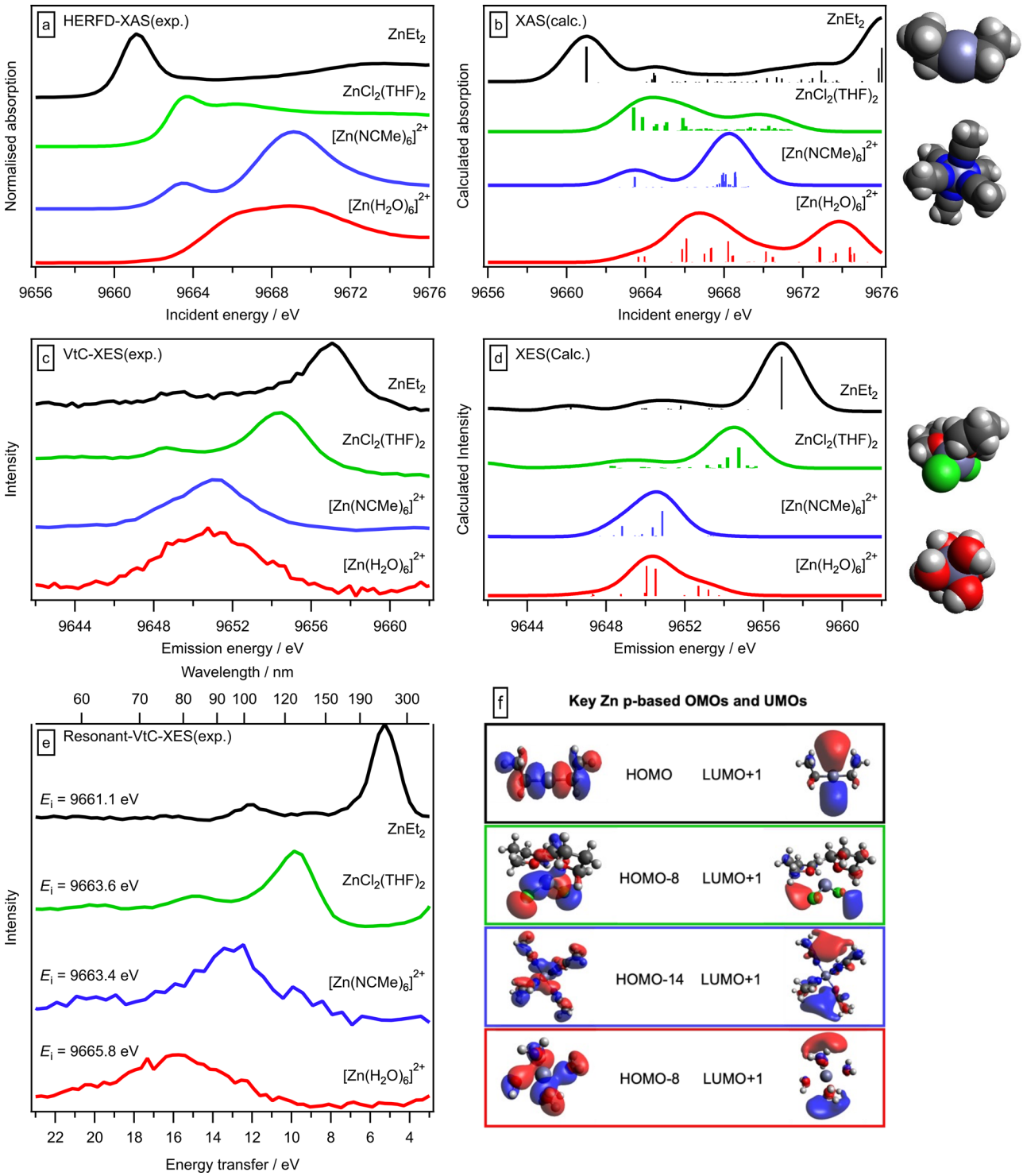

Fig. 3 | Zn 1s HERFD-XANES, NR-/R-VtC-XES, and DFT calculated spectra of $ZnEt_2$ and common zinc-containing compounds. 0.1 M $ZnEt_2$ in toluene, $ZnCl_2(THF)_2$ (0.1 M $ZnCl_2$ in THF), $[Zn(NCMe)_6]^{2+}$ (0.1 M $Zn(OTf)_2$ in MeCN) and $[Zn(OH_2)_6]^{2+}$ (0.1 M $ZnCl_2$ in H_2O): **a** Zn 1s HERFD-XANES spectra (y intensities normalised), **b** TDDFT calculations of Zn 1s HERFD-XANES (shifted by −8.90 eV to visually match experimental Zn 1s HERFD-XANES spectra[69]), **c** Zn 1s NR-VtC-XE spectra, **d** KS-DFT calculations of Zn 1s NR-VtC-XE spectra (shifted by −8.90 eV to visually match experimental Zn 1s NR-VtC-XE spectra). **e** R-VtC-XE spectra. **f** Visual representations for key Zn p-based OMOs and UMOs; for $ZnEt_2$ the LUMO + 2 is degenerate (or near-degenerate) with another UMO (Supplementary Fig. 8).

energy peak observed for all ZnR_2 in both the experimental (Fig. 3c, Fig. 4c) and calculated (Fig. 3d, Fig. 4d) Zn 1s NR-VtC-XE spectra (the selection rules for Zn 1s NR-VtC-XES are OMO,Zn p to Zn 1s[35,47,48]), along with a visual analysis of the MO, which shows a clear sigma bond along the axis of the linear C-Zn-C bonds (Fig. 3f, 4f). In contrast, for the 4/6-coordinate zinc-containing species, the main zinc contributions were for multiple OMOs far deeper than the HOMO, captured by the broader and lower energy peaks in Zn 1s NR-VtC-XE spectra (Fig. 3c), e.g. for $[Zn(OH_2)_6]^{2+}$ the HOMO-8 to HOMO-10 each had ~6% Zn p contribution (Supplementary Table 6). The OMO,Zn p is very likely to be more influential on

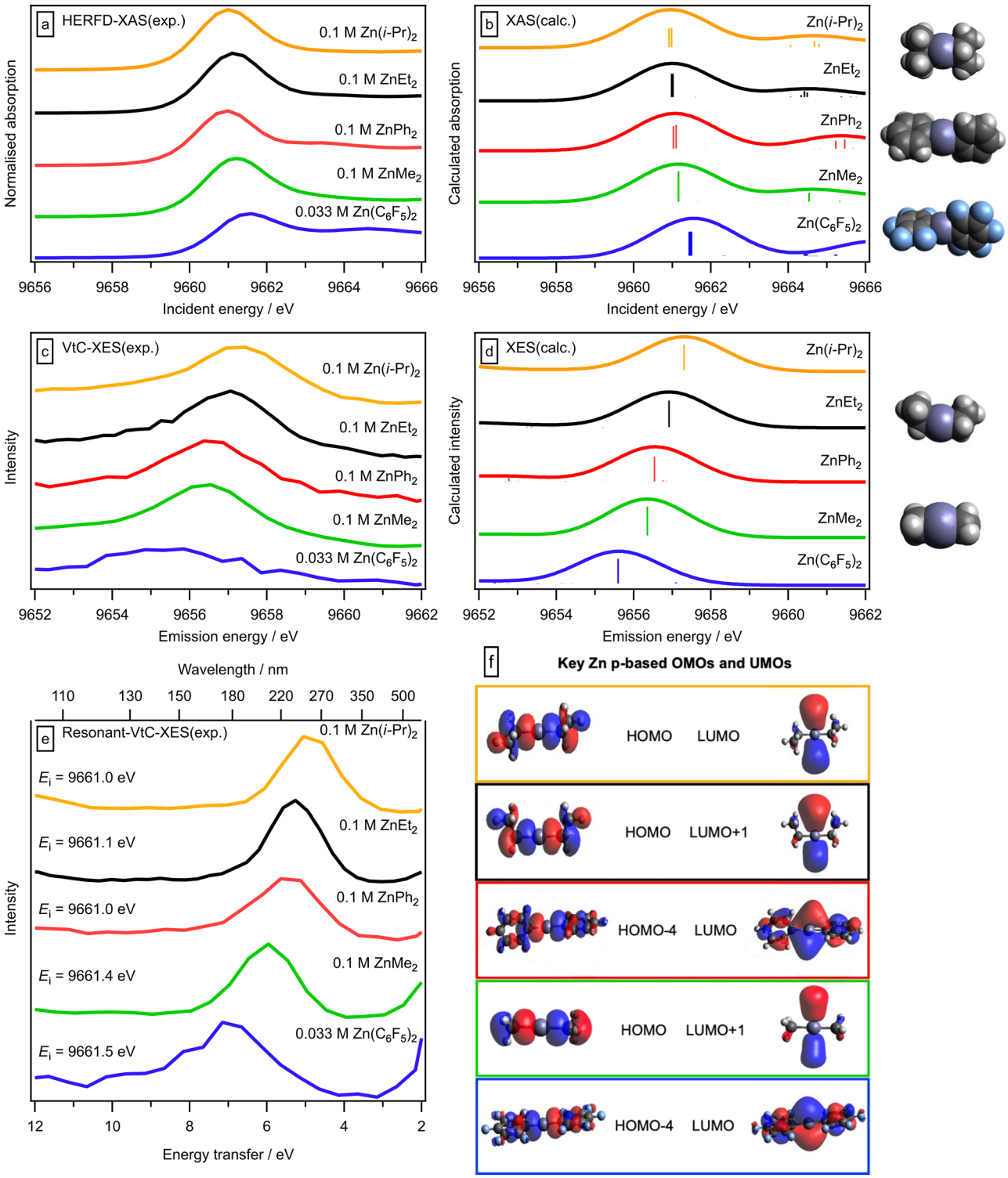

Fig. 4 | Zn 1s HERFD-XANES, NR-/R-VtC-XES, and DFT calculated spectra of ZnR_2 (R = Me, Et, *i*-Pr, C_6F_5) complexes. Experimental and calculated X-ray spectra for the diorganozinc compounds ZnR_2 (R = Me, Et, *i*-Pr, Ph, C_6F_5, concentration 0.1 M for all apart from C_6F_5 which was 0.033 M); calculated C_6F_5 shown here is the staggered conformer. **a** Zn 1s HERFD-XANES spectra (y intensities normalised), **b** TDDFT calculations of Zn 1s XANES spectra (shifted by −8.90 eV to visually match experimental Zn 1s HERFD-XANES spectra[69]), **c** Zn 1s NR-VtC-XE spectra, **d** KS-DFT calculations of Zn 1s NR-VtC-XE spectra (shifted by −8.90 eV to visually match experimental Zn 1s NR-VtC-XE spectra), **e** Zn 1s R-VtC-XE spectra, **f** Visual representations for key Zn p-based OMOs and UMOs; for ZnR_2 the UMO shown here is degenerate (or near-degenerate) with another UMO (Supplementary Fig. 8).

reactivity than OMO, Zn s, as the only OMO with a strong Zn s contribution is HOMO-1 for ZnR_2 (where R = alkyl) and HOMO-5 for ZnR_2 (where R = aryl) (Supplementary Figs. 25–28 and Supplementary Table 5), which are ~1.5 eV deeper than the single Zn p OMO.

The three lowest energy UMOs (LUMO, LUMO + 1 and LUMO + 2) for almost all ZnR_2, and also the common zinc-containing species, were composed of two Zn p-based UMOs and one Zn s-based UMO (Figs. 3f, 4f, Supplementary Figs. 9–24 and Supplementary Table 5). This identification

is based on a combination experimental and calculated Zn 1s HERFD-XANES spectra plus ground state DFT calculations. All three of these UMOs for ZnR_2 are similar in energy (Supplementary Figs. 25–28). The two degenerate (or near-degenerate) Zn p-containing UMOs have Zn p contributions of ~75% (R = alkyl) and ~40% (R = aryl), all perpendicular to C-Zn-C bond (Figs. 3f, 4f and Supplementary Table 5).

Our results demonstrate that Zn p orbitals contribute strongly to both OMOs and UMOs that are key in bond breaking and forming, contradicting theoretical findings which suggested that Zn p contributions could be neglected for zinc-containing species, including ZnR_2[62,63]. Furthermore, previous reports utilising a simplified hypervalent scheme, with no Zn p orbital contributions for $ZnMe_2$[63], were clearly too much of a simplification.

Overall, the UMOs for ZnR_2 are unremarkable compared to common zinc-containing species, highlighting that the electronically unusual states for ZnR_2 are the OMOs. Therefore, the strong reactivity of ZnR_2 compared to common zinc-containing species comes mainly from a combination of the OMOs and the two-coordinate structure.

Quantifying the effect of R on ZnR_2 reactivity: three new descriptors

To capture the zinc-specific, intrinsic *hardness*, η_{Zn}, our first new descriptor, we use the experimental Zn 1s R-VtC-XES peak energy (Fig. 2c), which represents the experimental energy gap between OMO,Zn p and UMO,Zn p, *E*(gap,exp). *E*(gap,exp) captures the Zn p-specific energy gap $\eta_{Zn} = E(\text{OMO,Zn p}) - E(\text{UMO,Zn p})$, where *E*(OMO,Zn p) and *E*(UMO,Zn p) represent the energies of the OMO and UMO with strongest Zn p contribution, respectively. Very importantly, the final-state electronic structure of R-VtC-XES is analogous to UV-Vis spectroscopy (Fig. 2d)[42], i.e. one electron in an UMO bound state and a hole in a valence OMO, but R-VtC-XES is an overall two-photon process which can bypass the dipole selection rules of UV-Vis spectroscopy to effectively access the optically dark Zn p to Zn p transitions. Therefore, our energy gap is essentially a zinc-specific, experimental version of the Pearson η (which is $\eta = (E(\text{HOMO}) - E(\text{LUMO}))/2$)[37]. A small zinc-specific η_{Zn} means relatively strong Zn-reactant molecule covalent interactions; large zinc-specific η_{Zn} means relatively strong Zn-reactant molecule electrostatic interactions, i.e. more ionic. In addition, we have used both DFT and multiconfigurational, multistate-restricted active space second-order perturbation theory (MS-RASPT2) calculations to guide our approach.

The experimental R-VtC-XES-derived descriptor η_{Zn} was: $Zn(C_6F_5)_2 \gg ZnMe_2 > ZnPh_2 > ZnEt_2 > Zn(i\text{-Pr})_2$ (Fig. 4e and Supplementary Fig. 29). Based on a combination of experimental and calculated data, the zinc-based η_{Zn} for ZnR_2 is: $Zn(C_6F_5)_2 > Zn(2,6\text{-}F_2C_6H_3)_2 > Zn(3,5\text{-}F_2C_6H_3)_2 > ZnMe_2 > ZnPh_2 > ZnEt_2 \approx Zn(n\text{-Pr})_2 \approx Zn(n\text{-Bu})_2 > Zn(i\text{-Pr})_2 > Zn(t\text{-Bu})_2$ (Fig. 5a). This experimental η_{Zn} can only be measured using R-VtC-XES as the experimental energy gaps for ZnR_2 correspond to ~175 nm to ~250 nm respectively (Fig. 4e), which cannot be measured using standard UV-Vis spectroscopy due to the energy gap being too large (for peaks up to ~200 nm) and the peaks being overwhelmed by the toluene solvent (for peaks up to ~285 nm)[64]. Furthermore, this experimental R-VtC-XES-derived η_{Zn} effectively captures a Zn p to Zn p transition, rather than the classic *E*(OMO) – *E*(UMO) energy gap measured using UV-Vis spectroscopy (Fig. 2d). MS-RASPT2 R-VtC-XES calculations, where the valence hole is included, match both the experimental R-VtC-XES energy gap order and absolute energy gap values for ZnR_2 (Fig. 6), demonstrating that the R-VtC-XES calculations capture the same physical effect as the experiments. Whilst an excellent match, these MS-RASPT2 calculations are time intensive and technically challenging. The ground state Zn p-specific $\eta_{Zn} = E(\text{OMO,Zn p}) - E(\text{UMO,Zn p})$ energy gap order (but not the absolute energies) is the same as observed using both experimental R-VtC-XES (Fig. 7a, $R^2 = 0.98$, Supplementary Fig. 32), demonstrating that the much cheaper and simpler ground state calculations capture η_{Zn}.

We calculate a zinc-specific, intrinsic *absolute electronegativity*, $\chi_{Zn} = (E(\text{OMO,Zn p}) + E(\text{UMO,Zn p}))/2$, our second new descriptor. These DFT calculations are validated against data from both Zn 1s HERFD-XANES spectroscopy and NR-VtC-XES (Fig. 3b, 3d); we have high confidence in given the excellent matches of our experimental and calculated spectra (Fig. 3 and Fig. 4). A large (or small) zinc-specific χ_{Zn} corresponds to a strong Lewis acidic (or Lewis basic) zinc centre.

Using both η_{Zn} and χ_{Zn}, a zinc-specific version of the global electrophilicity index (ω)[39,40], where $\omega_{Zn} = (\chi_{Zn})^2 / (2 \times \eta_{Zn})$, was calculated, our third new descriptor. A large (or small) zinc-specific ω_{Zn} corresponds to a strong Lewis acidic (or Lewis basic) zinc centre.

The zinc-specific descriptors χ_{Zn} and ω_{Zn} for ZnR_2 are: $Zn(C_6F_5)_2 > Zn(2,6\text{-}F_2C_6H_3)_2 > Zn(3,5\text{-}F_2C_6H_3)_2 > ZnPh_2 > ZnMe_2 > ZnEt_2 \approx Zn(n\text{-Pr})_2 \approx Zn(n\text{-Bu})_2 > Zn(i\text{-Pr})_2 > Zn(t\text{-Bu})_2$ (Fig. 5b, Fig. 5c, Supplementary Fig. 29 and Supplementary Table 7). χ_{Zn} and ω_{Zn} correlate linearly ($R^2 = 0.99$, Supplementary Fig. 33c), demonstrating that either can be used for quantifying Lewis acidity/basicity strength. Our results match quantitative reports on ZnR_2 and SacNacZnR Lewis acidity of $Zn(C_6F_5)_2 > ZnPh_2$[31,65]. Our results also match qualitative reports from empirical patterns of reactivity; $ZnEt_2$ as a relatively weak/mild Lewis acid[65] compared to $ZnPh_2$ and $Zn(C_6F_5)_2$[10,19], and $Zn(C_6F_5)_2$ as a strong Lewis acid[9,12]. Results from DFT calculations suggest that $ZnMe_2$ can act as a nucleophile[4]; our results show that any other ZnR_2 (where R = alkyl) would be a better nucleophile than $ZnMe_2$ (ignoring steric constraints).

Using zinc-specific η_{Zn}, χ_{Zn} and ω_{Zn} descriptors means we directly capture the electronic structure of the location where both electron acceptance (controlling Lewis acidity) and electron donation (controlling Lewis basicity[4]) occur for ZnR_2, i.e. the zinc centre. This approach removes the problem of ligand electronic contributions clouding production of the descriptors, ensuring that comparable and consistent values for different R substituents are produced. Furthermore, our zinc-specific approach means that the zinc spectroscopic contributions are not overwhelmed by solvent/ligand contributions.

The η_{Zn}, χ_{Zn} and ω_{Zn} descriptors show that strong Lewis acids are hard, and strong Lewis bases are soft. $Zn(C_6F_5)_2$ is a hard, strong Lewis acid/electrophile and $Zn(t\text{-Bu})_2$ is a soft, strong Lewis base/nucleophile.

χ_{Zn} and ω_{Zn} descriptors exhibit a strong correlation with the R Taft inductive substituent constant, I_R, for ZnR_2; as evidenced by a high R^2 value. (Supplementary Fig. 34 and Supplementary Table 7). The ability of substituent R to donate/withdraw electron density to/from the zinc centre explains ZnR_2 reactivity. The alkyl chain length makes very little difference for *n*-alkyl from Et onwards. This finding matches to results from gas-phase photoelectron spectroscopy of four ZnR_2 (R = alkyl)[38]. For the partially fluorinated Ph, χ_{Zn} increased fairly consistently with the increasing number of F substituents, e.g. $Zn(4\text{-}FC_6H_4)_2$ has a smaller χ_{Zn} than $Zn(3,5\text{-}F_2C_6H_3)_2$; the positioning of the fluorine on aryl matters: *ortho* has the largest effect relative to $ZnPh_2$, with a weaker effect for *meta* (Supplementary Fig. 29).

η_{Zn}, χ_{Zn} and ω_{Zn} descriptors have almost the same order (Fig. 5a-c, Supplementary Fig. 33), and correlate well with *E*(gap,exp) (Fig. 7). Therefore, our *experimentally measured* R-VtC-XES Zn p-specific energy gap *E*(gap,exp), i.e. η_{Zn}, can be used with a good level of confidence as a single experimental descriptor to quantify the effect of substituent R on ZnR_2 reactivity. Furthermore, η_{Zn}, χ_{Zn} and ω_{Zn} descriptors are influenced strongly by *E*(OMO,Zn p) (Fig. 5 and Supplementary Fig. 35). Therefore, *E*(OMO,Zn p) can be used as a single descriptor to quantify the effect of substituent R on ZnR_2 reactivity; *E*(OMO,Zn p) can be readily calculated—a ground state DFT calculation, then straightforward visual identification of OMO Zn p for ZnR_2—allowing accessible in silico screening of ZnR_2 species. Even simpler, χ_{Zn} and ω_{Zn} can be predicted if the induction ability of the R substituent is known (Supplementary Fig. 34).

Conclusions and future work

Our combination of three synchrotron-based, solution-phase, zinc-specific *X-ray spectroscopies* coupled with calculations allows the comprehensive, systematic and quantitative elucidation of the electronic properties that define the reactivity of synthetically-relevant ZnR_2. We have unambiguously and directly demonstrated that a range of ZnR_2 reagents, in the solvents toluene and hexane, adopt a linear two-coordinate geometry, which

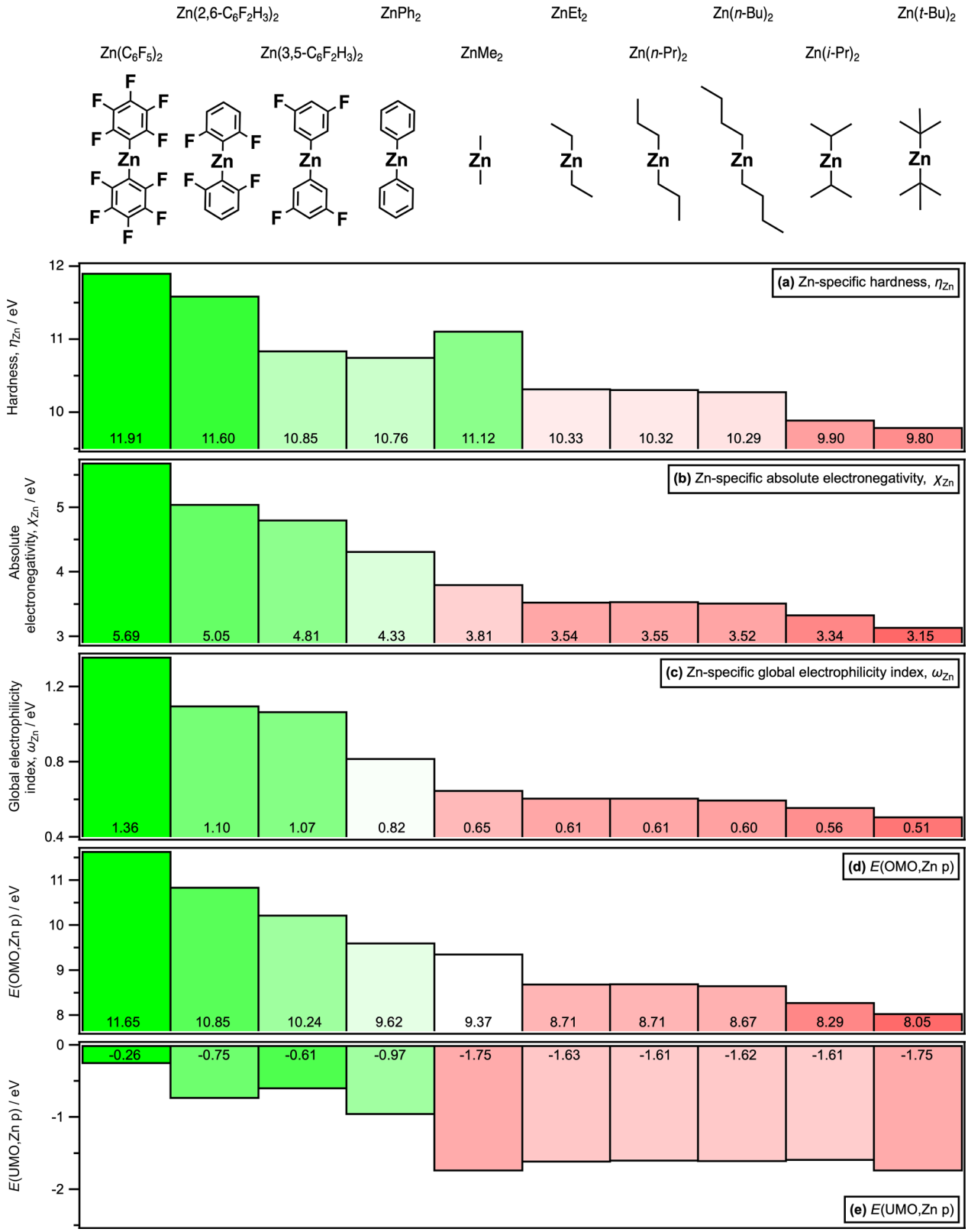

Fig. 5 | Computed Zn-specific electronic structure descriptors: η_{Zn}, χ_{Zn}, ω_{Zn}, *E*(OMO,Zn p), and *E*(UMO,Zn p). Electronic structure properties for ZnR_2: **a** zinc-specific hardness (η_{Zn}), **b** zinc-specific absolute electronegativity (χ_{Zn}), **c** zinc-specific global electrophilicity index (ω_{Zn}), **d** *E*(OMO,Zn p), **e** *E*(UMO,Zn p). Tabulated values available in Supplementary Table 7.

establishes that electronic structure will be the primary controller of reactivity. We provide new, intrinsic, quantitative Lewis acidity/basicity descriptors for liquid-phase ZnR_2 compounds, which opens up the possibility of fine-tuning ZnR_2 reactivity and greatly reduces the need for empirical, iterative synthetic experimentation. Zinc-specific hardness, equivalent to the experimental energy gap between OMO,Zn p and UMO,Zn p, quantifies the chances of forming a more covalent or electrostatic bond with a reactant molecule. Zinc-specific absolute electronegativity

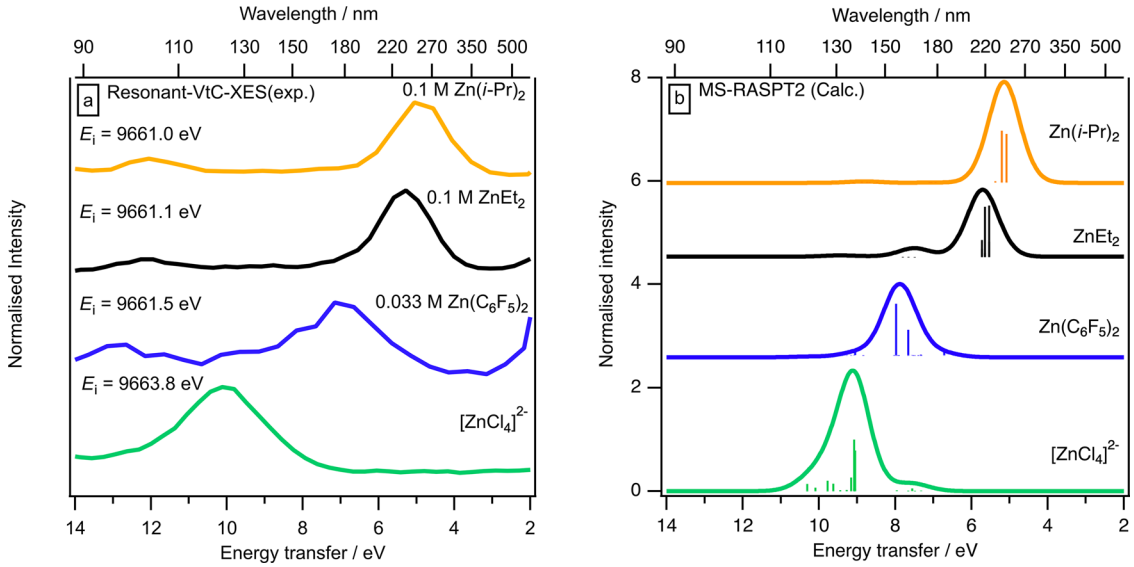

Fig. 6 | Experimental and calculated spectra of ZnR_2 (R = Me, Et, *i*-Pr, C_6F_5) and $[ZnCl_4]^{2-}$. Comparison of experimental and calculated R-VtC-XE spectra: **a** experimental spectra for ZnR_2 (R = Me, Et, *i*-Pr and C_6F_5; concentration 0.1 M for all except C_6F_5, which was 0.03 M) and $x = 0.33$ $ZnCl_2$ in $[C_8C_1Im]Cl$ (which gives only $[ZnCl_4]^{2-}$ in solution[47,69]); **b** Calculated RASPT2 (MS-RASPT2(12,1,1;1,5,3) ANO-RCC-VTZP) spectra for ZnR_2 (R = Et, *i*-Pr and C_6F_5; the staggered conformer of C_6F_5 was used) and $[ZnCl_4]^{2-}$. All calculated spectra include Gaussian broadening with a full width at half maximum (FWHM) of 2.5 eV.

and zinc-specific global electrophilicity index both quantify electron acceptor (*i.e.* Lewis acidity/electrophilicity) and electron donor (i.e. nucleophilicity/nucleophilicity) abilities. For rapid screening, both the induction strength of the R substituents of ZnR_2 and the energy of the calculated OMO,Zn p, *E*(OMO,Zn p), are excellent descriptors for quantification of both zinc-specific hardness and absolute electronegativity, of potential use within the wider catalysis and FLP communities. These new empirical zinc-specific descriptors also provide excellent inputs for quantitative structure-property relationships (QSAR) or for reaction discovery/development using automated synthesis machines.

A combination of factors give rise to the remarkable reactivity of ZnR_2 over common zinc-containing species. Firstly, the easily ionised Zn p-containing OMO; secondly, ZnR_2 electronic softness; thirdly, the sterically accessible Zn p-containing UMOs due to the linear ZnR_2 geometric structure.

Our *liquid-phase* and *zinc-specific* suite of X-ray spectroscopy techniques allow us to side-step many common spectroscopic issues for zinc in solution. Zn 1s R-VtC-XES, which we demonstrate the use of for the first time here, is incredibly powerful for studying zinc as we can *exclusively* focus on the electronic structure associated with the zinc centre rather than that of the associated ligands. R-VtC-XES effectively provides a *zinc-specific* version (with different selection rules) of UV-Vis spectroscopy that avoids the classic problems of solvent windows or ligand absorption. Therefore, R-VtC-XES is suitable for a vast range of functional zinc species, from enzymes through to batteries and under the diverse conditions they would encounter. In the area of organometallics, future work could focus on donor/coordinating solvents[60], potentially intramolecularly coordinating R substituents (e.g. $Zn[(CH_2)_3X]_2$ where $X = SCH_3$, $N(CH_3)_2$)[66], zincates/dinuclear complexes[67], and zinc bis-amides[68].

Our *liquid-phase* and *element-specific* suite of X-ray spectroscopy techniques offers exceptional opportunities for capturing geometric and electronic structure and producing descriptors for interpreting and predicting reactivity, for the first time for many elements. Plenty of XANES, NR-VtC-XES and R-VtC-XES studies exist for fourth period (i.e. first row) transition metals[42,43,49–52], but studies for other elements are limited. Elements for which this approach is particularly attractive are those with oxidation states that give closed-shell d^{10}, where p orbitals are crucial for bonding, i.e. main-group elements in the latter part of the fourth period and the start of the fifth period: Ga, Ge, As, Se, Br, Rb, Sr.

Methods

Sample preparation

All samples were prepared in a glove box, under inert conditions (nitrogen, $H_2O < 0.1$ ppm, $O_2 < 0.5$ ppm). 1 M diethylzinc ($ZnEt_2$) in hexanes, 2 M dimethylzinc ($ZnMe_2$) in toluene, 1 M di*iso*propylzinc ($Zn(i\text{-}Pr)_2$) in toluene, diphenylzinc ($ZnPh_2$) (98%), bis(pentafluorophenyl)zinc ($Zn(C_6F_5)_2$) (98%), anhydrous zinc trifluoromethanesulfonate ($Zn(TfO)_2$) (98%), and anhydrous zinc chloride ($ZnCl_2$) (99%) were obtained from Sigma-Aldrich. 1-octyl-3-methylimidazolium chloride ($[C_8C_1Im]Cl$) (99%) was obtained from Iolitec. Neat solvents toluene, tetrahydrofuran and acetonitrile were obtained from Sigma-Aldrich. To avoid self-absorption, solutions were made/diluted to 0.1 M. $Zn(C_6F_5)_2$ was prepared at 0.033 M due to the presence of insoluble matter at 0.1 M. Zinc tetrachloride, $[ZnCl_4]^{2-}$, was prepared from a mixture of $ZnCl_2$ (0.838 g, 6.15 mmol) in $[C_8C_1Im]Cl$ (2.882 g, 12.49 mmol) to the desired mole fraction $x = 0.33$, i.e. $2 \times [C_8C_1Im]Cl + ZnCl_2 \rightarrow [C_8C_1Im]_2[ZnCl_4]$, following literature procedures[47,69]. The samples were prepared within plastic centrifuge vials (*ca.* 0.5 ml to 1.0 ml), sealed, and transported to the I20-Scanning experimental hutch. The samples were held in front of the X-ray beam either in a small plastic vice at the top and bottom; or the centrifuge vial was held with a small ring (Supplementary Fig. 36).

HERFD-XAS experiments

X-ray absorption (XA) spectra were collected at Diamond Light source I20-Scanning[70]. A Si(111) four-bounce monochromator (energy range: Si(111): incident energy, $E_i = 4$ eV to 20 keV; energy resolution: $\delta E/E = 1.3\times10^{-4}$) was used to scan from $E_i = 9600$ eV to 9900 eV. XA spectra were collected using an X-ray emission spectrometer[71], and by fixing the emission energy to monitor the relaxation of the $K\beta_{1,3}$ emission line at emission energy, $E_e = 9572$ eV. Scanning parameters were as follows: the pre-edge region ($E_i = 9600$ eV to 9650 eV) in 5.0 eV steps, the edge region $E_i = 9650$ eV to 9675 eV) in 0.3 eV steps, and the post-edge region ($E_i = 9675$ eV to 9698 eV) in 0.6 eV steps, and the post-XANES region ($E_i = 9698$ eV to 9750 eV in 1.6 eV steps; $E_i = 9750$ eV to 9900 eV in 2.0 eV steps, respectively). Samples were orientated at a 90° angle with respect to the incident beam at ambient temperature and pressure. Incident beam flux was lowered through attenuation (aluminium 0.2 mm, carbon 2.0 mm) to minimise radiation damage. XANES spectra were monitored throughout all scans to determine any degradation or damage to the sample over time. The energy of the

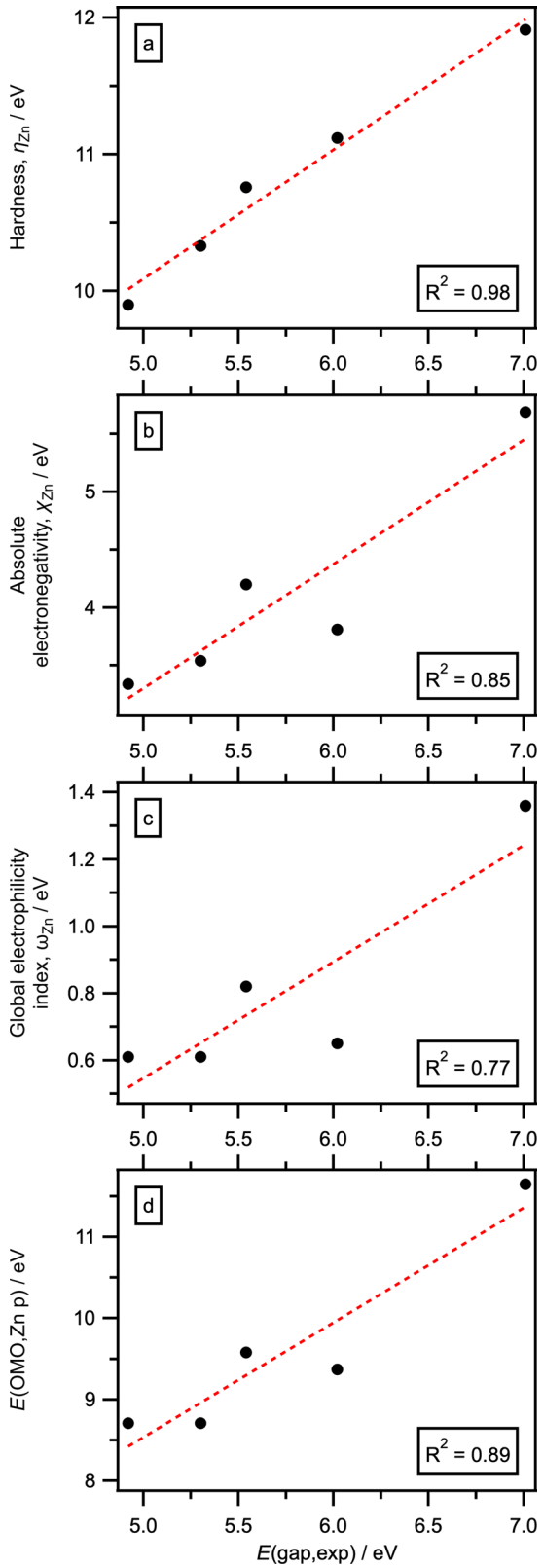

Fig. 7 | Computed Zn-specific descriptor correlations with experimental R-VtC-XES gap. Linear correlation fits for calculated descriptors against experimental R-VtC-XES energy gap (E(gap,exp)): **a** zinc-specific hardness (η_{Zn}) versus E(gap,exp); **b** zinc-specific absolute electronegativity (χ_{Zn}) versus E(gap,exp); **c** zinc-specific global electrophilicity index (ω_{Zn}) versus E(gap,exp) and **d** E(OMO,Zn p) versus E(gap,exp).

monochromator was calibrated to the Zn K-edge of a Zn foil (9659.0 eV) (Supplementary Fig. 37).

XES experiments

X-ray emission (XE) spectra were collected using the X-ray emission spectrometer at Diamond Light source I20-Scanning using three Ge(555) crystal to record the $K\beta_{2,5}$ emission line, i.e. valence-to-core (VtC). For NR-VtC-XE spectra, the incident energy was set to E_i = 9800 eV, significantly above resonant conditions. For the R-VtC-XE experiments, the incident energy was set to the white-line intensity (near-edge region absorption maxima). Resonant and non-resonant VtC XE spectra were recorded over the emission energy range, E_e = 9630 eV to 9700 eV.

Data processing

Experimental XA spectra were averaged and normalised using the Demeter software package, Athena[72]. NR-VtC-XES and R-VtC-XES data processing were performed using Igor Pro 8.0. The recorded emission spectra were adjusted to account for the incident beam energy calibration, ensuring accurate emission energy alignment. This was achieved by fitting a Gaussian distribution to the recorded elastic peak and adjusting so that the emission energy subtracted from incident energy equals zero. This shift was applied to all recorded emission spectra, assuming the spectrometer remained stable during the measurement of each solution studied (Supplementary Table 8).

Calculations

Geometry optimisations

All calculations were performed using the ORCA 5.0.3 electronic structure program[73]. Cartesian coordinates for all complexes were built using Avogadro[74]. Geometry optimisations were performed with tight convergence, an ultrafine grid (defgrid3) and without symmetry constraints using a range-separated hybrid functional, ωB97X-D3BJ[75], with a modified ZORA-def2-TZVPP basis set[76], paired with a decontracted SARC/J auxiliary basis set[77]. The RIJCOSX approximation was used to speed up optimisations. Scalar relativistic effects were introduced using the zeroth-order regular approximation (ZORA)[78]. Dispersion effects were taken into account using the atom-pairwise dispersion correction with the Becke-Jonson damping scheme. The solvent environment was modelled using the Conductor-like Polarisable Continuum Model (CPCM)[79,80], *via* the PCM implicit solvent models for toluene, hexane, water, acetonitrile (MeCN), tetrahydrofuran (THF) and ionic liquid (relative permittivity = 11.40)[81], respectively. Frequency analysis was carried out for all optimised structures, which are confirmed as minima by the absence of imaginary modes. Avogadro was used as an aid in the quantitative analysis of ORCA output files and the visualisation of molecular orbitals.

XAS and XES calculations

All calculations were performed using the ORCA 5.0.3 electronic structure program[73]. Single point calculations utilising a larger basis set to better capture the electronic structure were performed with time-dependent DFT for XAS and Kohn-Sham DFT for XES, using the ωB97X-D3BJ functional, with a ZORA-def2-QZVPP basis set[76] and SARC/J auxiliary basis set[77]. In all cases, electric-dipole, magnetic-dipole, and quadrupole contributions were allowed in spectral calculations. Time-dependent DFT calculations were performed with the Tamm-Dancoff approximation (TDA) applied. The solvent environment was modelled using the Conductor-like Polarisable Continuum Model (CPCM)[79,80], *via* the PCM implicit solvent models for toluene, hexane, water, acetonitrile (MeCN), tetrahydrofuran (THF) and ionic liquid (relative permittivity = 11.40)[81], respectively. For the XAS calculation, the Zn 1s orbital was excited into all virtual UMOs to mimic the Zn 1s K-edge XAS. Calculated XAS spectra were shifted by −8.90 eV to align with the experimental energies (Supplementary Fig. 38). Ground-state KS-DFT VtC-XES calculations were performed. A single relative shift of

−8.90 eV was applied from the difference between the most intense VtC peak in the experiment and the calculation (Supplementary Fig. 39). All computational spectra were generated by convoluting the computed energies and oscillator strengths with Gaussian functions with a full width at half maximum (FWHM) of 2.50 eV.

MS-RASPT2 calculations

RXES spectra were calculated with the state-averaged restricted active space self-consistent field (SA- RASSCF)[82,83] method with multi-state restricted active space second-order perturbation theory (MS-RASPT2)[84,85]. Calculations were performed in OpenMolcas[86], where the core-hole states are generated using the highly excited state scheme (HEXS)[87] and the transition energies and dipole vectors between states are calculated across a set of biorthonormal orbitals using the restricted active space state interaction method[88]. All calculations use the ANO-RCC-VTZP basis set, which includes relativistic effects[89–92], and an imaginary shift of 0.1 a.u. was applied to the MS-RASPT2 calculation to remove intruder states. Solvent effects were included using the implicit PCM solvent model for toluene and ionic liquid (relative permittivity = 11.40)[81]. To maintain a consistent level of theory, the RXES calculations of the different zinc complexes use the same active space size. The Zn 1s orbital was placed into RAS1 (maximum number of holes restricted to 1), the highest 5 occupied orbitals were placed into RAS2 (full CI space) and the lowest three unoccupied orbitals were placed into RAS3 (maximum number of electrons restricted to 1). 3 core excited and 15 valence excited states were included in each calculation and approximate relative RIXS intensities were calculated using a previously used simplified formalism of the Kramer-Heisenberg equation which assumes resonant conditions and a constant lifetime-broadening broadening[93–95].

Calculation processing

MOAnalyzer was employed to determine the percentage contribution of Zn s/p character within key molecular orbitals involved in both XAS and XES calculations using Löwdin population analysis[96]. MultiWFN was used to visualise the molecular orbitals constituting the occupied valence states[97]; this was achieved by analysing the total density-of-states (tDoS) and partial density-of-states (pDoS), specifically fragmenting both the Zn s/p orbitals.

Data availability

Raw data were collected using the I20-Scanning beamline at Diamond Light Source. Raw data and calculation output files supporting the findings of this study are available at University of Reading Research Data Archive, https://doi.org/10.17864/1947.001460. Calculations performed using ORCA can be reproduced using the provided coordinates and example input files included in the supplementary information. MS-RASPT2 calculation input files can be requested from A.E.A.F.

Received: 26 February 2025; Accepted: 10 September 2025;
Published online: 03 October 2025

References

1. Erdik, E. Organozinc Reagents in Organic Synthesis. (CRC Press, 1996).
2. Knochel, P. & Jones, P. *Organozinc Reagents*. (Oxford University Press, 1999).
3. Seyferth, D. Zinc alkyls, Edward Frankland, and the beginnings of main-group organometallic chemistry. *Organometallics* **20**, 2940–2955 (2001).
4. del Pozo, J., Gioria, E., Casares, J. A., Alvarez, R. & Espinet, P. Organometallic nucleophiles and Pd: What makes $ZnMe_2$ different? Is Au like Zn? *Organometallics* **34**, 3120–3128 (2015).
5. Alexakis, A., Bäckvall, J. E., Krause, N., Pàmies, O. & Diéguez, M. Enantioselective copper-catalyzed conjugate addition and allylic substitution reactions. *Chem. Rev.* **108**, 2796–2823 (2008).
6. Pu, L. & Yu, H. B. Catalytic asymmetric organozinc additions to carbonyl compounds. *Chem. Rev.* **101**, 757–824 (2001).
7. Yamada, K. & Tomioka, K. Copper-catalyzed asymmetric alkylation of imines with dialkylzinc and related reactions. *Chem. Rev.* **108**, 2874–2886 (2008).
8. Müller, D. S. & Marek, I. Asymmetric copper-catalyzed carbozincation of cyclopropenes en route to the formation of diastereo- and enantiomerically enriched polysubstituted cyclopropanes. *J. Am. Chem. Soc.* **137**, 15414–15417 (2015).
9. Hernán-Gómez, A. et al. Exploiting synergistic effects in organozinc chemistry for direct stereoselective *C*-glycosylation reactions at room temperature. *Angew. Chem. Int. Ed.* **57**, 10630–10634 (2018).
10. Borys, A. M., Gil-Negrete, J. M. & Hevia, E. Atom-efficient transition-metal-free arylation of *N,O*-acetals using diarylzinc reagents through Zn/Zn cooperativity. *Chem. Commun.* **57**, 8905–8908 (2021).
11. Dunsford, J. J., Clark, E. R. & Ingleson, M. J. Direct C(sp^2)-C(sp^3) cross-coupling of diaryl zinc reagents with benzylic, primary, secondary, and tertiary alkyl halides. *Angew. Chem. Int. Ed.* **54**, 5688–5692 (2015).
12. Borys, A. M., Kunzmann, T., Gil-Negrete, J. M. & Hevia, E. Atom-efficient arylation of N-tosylimines mediated by cooperative ZnAr2/Zn(C6F5)(2) combinations. *Chem. Commun.* **59**, 7583–7586 (2023).
13. Pike, S. D., White, E. R., Shaffer, M. S. P. & Williams, C. K. Simple phosphinate ligands access zinc clusters identified in the synthesis of zinc oxide nanoparticles. *Nat. Commun.* **7**, 13008 (2016).
14. Weckman, T. & Laasonen, K. Atomic layer deposition of zinc oxide: diethyl zinc reactions and surface saturation from first-principles. *J. Phys. Chem. C.* **120**, 21460–21471 (2016).
15. Li, X. Q., Wang, B., Ji, H. Y. & Li, Y. S. Insights into the mechanism for ring-opening polymerization of lactide catalyzed by $Zn(C_6F_5)_2$/organic superbase Lewis pairs. *Catal. Sci. Technol.* **6**, 7763–7772 (2016).
16. Piedra-Arroni, E., Ladaviere, C., Amgoune, A. & Bourissou, D. Ring-opening polymerization with $Zn(C_6F_5)_2$-based Lewis pairs: original and efficient approach to cyclic polyesters. *J. Am. Chem. Soc.* **135**, 13306–13309 (2013).
17. Neu, R. C., Otten, E. & Stephan, D. W. Bridging binding modes of phosphine-stabilized nitrous oxide to $Zn(C_6F_5)_2$. *Angew. Chem. Int. Ed.* **48**, 9709–9712 (2009).
18. Liberman-Martin, A. L., Levine, D. S., Ziegler, M. S., Bergman, R. G. & Tilley, T. D. Lewis acid-base interactions between platinum(II) diaryl complexes and bis(perfluorophenyl)zinc: strongly accelerated reductive elimination induced by a Z-type ligand. *Chem. Commun.* **52**, 7039–7042 (2016).
19. Wang, B., Wei, Y., Li, Z. J., Pan, L. & Li, Y. S. From $Zn(C_6F_5)_2$ to $ZnEt_2$-based Lewis pairs: significantly improved catalytic activity and monomer adaptability for the ring-opening polymerization of lactones. *ChemCatChem* **10**, 5287–5296 (2018).
20. Paterson, A. F. et al. Addition of the Lewis acid $Zn(C_6F_5)_2$ enables organic transistors with a maximum hole mobility in excess of 20 $cm^2 V^{-1} s^{-1}$. *Adv. Mater.* **31**, 1900871 (2019).
21. Huo, H. H., Gorsline, B. J. & Fu, G. C. Catalyst-controlled doubly enantioconvergent coupling of racemic alkyl nucleophiles and electrophiles. *Science* **367**, 559–564 (2020).
22. McCann, L. C. & Organ, M. G. On the remarkably different role of salt in the cross-coupling of arylzincs from that seen with alkylzincs. *Angew. Chem. Int. Ed.* **53**, 4386–4389 (2014).
23. Fischer, C. & Fu, G. C. Asymmetric nickel-catalyzed negishi cross-couplings of secondary α-bromo amides with organozinc reagents. *J. Am. Chem. Soc.* **127**, 4594–4595 (2005).
24. Knochel, P. & Singer, R. D. Preparation and reactions of polyfunctional organozinc reagents in organic synthesis. *Chem. Rev.* **93**, 2117–2188 (1993).
25. Haas, D., Hammann, J. M., Greiner, R. & Knochel, P. Recent developments in Negishi cross-coupling reactions. *Acs Catal* **6**, 1540–1552 (2016).

26. *Asymmetric Autocatalysis: The Soai Reaction* (eds Soai, K., Kawasaki, T. & Matsumoto, A.) (The Royal Society of Chemistry, 2022).
27. *Zinc Catalysis: Applications in Organic Synthesis* (eds Enthaler, S. & Wu, X. F.) (Wiley-VCH, Weinheim, 2015).
28. Jochmann, P. & Stephan, D. W. Reactions of CO_2 with heteroleptic zinc and zinc-NHC complexes. *Organometallics* **32**, 7503–7508 (2013).
29. Tulewicz, A. et al. Towards extended zinc ethylsulfinate networks by stepwise insertion of sulfur dioxide into Zn-C bonds. *Chem. -Eur. J.* **25**, 14072–14080 (2019).
30. Procter, R. J., Uzelac, M., Cid, J., Rushworth, P. J. & Ingleson, M. J. Low-coordinate NHC-zinc hydride complexes catalyze alkyne C-H borylation and hydroboration using pinacolborane. *Acs Catal* **9**, 5760–5771 (2019).
31. Allen, J. et al. Organozinc β-thioketiminate complexes and their application in ketone hydroboration catalysis. *Organometallics* **44**, 749–759 (2025).
32. Specklin, D., Fliedel, C. & Dagorne, S. Recent representative advances on the synthesis and reactivity of *N*-heterocyclic-carbene-supported zinc complexes. *Chem. Rec.* **21**, 1130–1143 (2021).
33. Hevia, E. & Dankert, F. Reductive-transmetalation reactions of ZnR_2/$(AlCp^*)_4$ heterobimetallic combinations and application towards CO_2 insertion. *Eur. J. Inorg. Chem.* **27**, e202400418 (2024).
34. Penner-Hahn, J. E. Characterization of "spectroscopically quiet" metals in biology. *Coord. Chem. Rev.* **249**, 161–177 (2005).
35. Stepanic, O. M. et al. Probing a silent metal: a combined X-ray absorption and emission spectroscopic study of biologically relevant zinc complexes. *Inorg. Chem.* **59**, 13551–13560 (2020).
36. Erdmann, P. & Greb, L. What distinguishes the strength and the effect of a lewis acid: analysis of the Gutmann-Beckett method. *Angew. Chem. Int. Ed.* **61**, e202114550 (2022).
37. Pearson, R. G. Absolute electronegativity and hardness—application to inorganic chemistry. *Inorg. Chem.* **27**, 734–740 (1988).
38. Haaland, A. et al. The length, strength and polarity of metal-carbon bonds: dialkylzinc compounds studied by density functional theory calculations, gas electron diffraction and photoelectron spectroscopy. *Dalton Trans*. 4356-4366 (2003).
39. Jupp, A. R., Johnstone, T. C. & Stephan, D. W. The global electrophilicity index as a metric for Lewis acidity. *Dalton Trans* **47**, 7029–7035 (2018).
40. Jupp, A. R., Johnstone, T. C. & Stephan, D. W. Improving the global electrophilicity index (GEI) as a measure of Lewis acidity. *Inorg. Chem.* **57**, 14764–14771 (2018).
41. Seidel, R., Winter, B. & Bradforth, S. E. Valence electronic structure of aqueous solutions: insights from photoelectron spectroscopy. *Annu. Rev. Phys. Chem.* **67**, 283–305 (2016).
42. Glatzel, P., Sikora, M., Smolentsev, G. & Fernandez-Garcia, M. Hard X-ray photon-in photon-out spectroscopy. *Catal. Today* **145**, 294–299 (2009).
43. Bauer, M. HERFD-XAS and valence-to-core-XES: new tools to push the limits in research with hard X-rays? *Phys*. *Chem. Chem. Phys.* **16**, 13827–13837 (2014).
44. Nchari, L. N. et al. In *14th International Conference on X-Ray Absorption Fine Structure* Vol. 190 Journal of Physics Conference Series (eds DiCicco, A. & Filipponi, A.) (Iop Publishing Ltd, 2009).
45. Werner, T., Bauer, M., Riahi, A. M. & Schramm, H. A catalytic system for the activation of diorganozinc reagents. *Eur. J. Org. Chem* **2014**, 4876–4883 (2014).
46. Brown, N. J. et al. From organometallic zinc and copper complexes to highly active colloidal catalysts for the conversion of CO_2 to methanol. *Acs Catal* **5**, 2895–2902 (2015).
47. Clarke, C. J. et al. Zinc 1s valence-to-core X-ray emission spectroscopy of halozincate complexes. *J. Phys. Chem. A* **123**, 9552–9559 (2019).
48. Dhakal, D. et al. The evolution of solvation symmetry and composition in Zn halide aqueous solutions from dilute to extreme concentrations. *Phys. Chem. Chem. Phys.* **25**, 22650–22661 (2023).
49. Glatzel, P. & Bergmann, U. High resolution 1s core hole X-ray spectroscopy in 3d transition metal complexes - electronic and structural information. *Coord. Chem. Rev.* **249**, 65–95 (2005).
50. Pollock, C. J. & DeBeer, S. Insights into the geometric and electronic structure of transition metal centers from valence-to-core X-ray emission spectroscopy. *Acc. Chem. Res.* **48**, 2967–2975 (2015).
51. Kowalska, J. K., Lima, F. A., Pollock, C. J., Rees, J. A. & DeBeer, S. A practical guide to high-resolution X-ray spectroscopic measurements and their applications in bioinorganic chemistry. *Isr. J. Chem.* **56**, 803–815 (2016).
52. MacMillan, S. N. & Lancaster, K. M. X-ray spectroscopic interrogation of transition-metal-mediated homogeneous catalysis: primer and case studies. *Acs Catal* **7**, 1776–1791 (2017).
53. Rio, J., Perrin, L. & Payard, P. A. Structure-reactivity relationship of organozinc and organozincate reagents: key elements towards molecular understanding. *Eur. J. Org. Chem* **2022**, e202200906 (2022).
54. Markies, P. R. et al. Coordinational behavior of solvent-free diorganylzinc compounds - the remarkable X-ray structure of dimeric diphenylzinc. *Organometallics* **9**, 2243–2247 (1990).
55. *The Chemistry of Organozinc Compounds* (eds Rappoport, Z. & Marek, I.) (John Wiley & Sons, Chichester, 2006).
56. Crockett, M. P., Zhang, H., Thomas, C. M. & Byers, J. A. Adding diffusion ordered NMR spectroscopy (DOSY) to the arsenal for characterizing paramagnetic complexes. *Chem. Commun.* **55**, 14426–14429 (2019).
57. Evans, R. The interpretation of small molecule diffusion coefficients: quantitative use of diffusion-ordered NMR spectroscopy. *Prog. Nucl. Magn. Reson. Spectrosc.* **117**, 33–69 (2020).
58. Baker, M. L. et al. K- and L-edge X-ray absorption spectroscopy (XAS) and resonant inelastic X-ray scattering (RIXS) determination of differential orbital covalency (DOC) of transition metal sites. *Coord. Chem. Rev.* **345**, 182–208 (2017).
59. Bacsa, J. et al. The solid-state structures of dimethylzinc and diethylzinc. *Angew. Chem. Int. Ed.* **50**, 11685–11687 (2011).
60. del Pozo, J. et al. Speciation of $ZnMe_2$, ZnMeCl, and $ZnCl_2$ in tetrahydrofuran (THF), and its influence on mechanism calculations of catalytic processes. *Acs Catal* **7**, 3575–3583 (2017).
61. Fazekas, E., Lowy, P. A., Rahman, M. A. & Garden, J. A. In *Comprehensive Organometallic Chemistry IV (Fourth Edition)* Vol. 11 (ed Liptrot, D. J.) 193-304 (Elsevier Ltd., 2022).
62. Daniel, A. G. & Farrell, N. P. The dynamics of zinc sites in proteins: electronic basis for coordination sphere expansion at structural sites. *Metallomics* **6**, 2230–2241 (2014).
63. Mirabi, B., Poh, W. C., Armstrong, D., Lough, A. J. & Fekl, U. Why diorganyl zinc lewis acidity dramatically increases with narrowing C-Zn-C bond angle. *Inorg. Chem.* **59**, 2621–2625 (2020).
64. Reichardt, C. & Welton, T. *Solvents and Solvent Effects in Organic Chemistry*. 4th edn, (Wiley, 2011).
65. Jana, R., Pathak, T. P. & Sigman, M. S. Advances in transition metal (Pd,Ni,Fe)-catalyzed cross-coupling reactions using alkyl-organometallics as reaction partners. *Chem. Rev.* **111**, 1417–1492 (2011).
66. Dekker, J., Boersma, J., Fernholt, L., Haaland, A. & Spek, A. L. Molecular-structures of bis(3-(dimethylamino)propyl)zinc, $Zn((CH_2)_3N(CH_3)_2)_2$, by X-ray and gas electron-diffraction and bis(3-mercaptopropyl)zinc, $Z((CH_2)_3SCH_3)_2$, by gas electron-diffraction. *Organometallics* **6**, 1202–1206 (1987).
67. Pierret, A., Lefebvre, C., Gros, P. C., Denhez, C. & Vasseur, A. The mechanism of lithium zincate-mediated I/Zn exchange revisited: a computational microsolvation approach in THF. *Eur. J. Org. Chem.* **26**, 13 (2023).

68. Judge, N. R. & Hevia, E. Alkali-metal-alkoxide powered zincation of fluoroarenes employing zinc bis-amide $Zn(TMP)_2$. *Angew. Chem. Int. Ed* **62**, 7 (2023).
69. Seymour, J. M. et al. Unravelling the complex speciation of halozincate ionic liquids using X-ray spectroscopies and calculations. *Faraday Discuss* **253**, 251–272 (2024).
70. Diaz-Moreno, S. et al. In *14th International Conference on X-Ray Absorption Fine Structure* Vol. 190 *Journal of Physics Conference* Series (eds DiCicco, A. & Filipponi, A.) (Iop Publishing Ltd, 2009).
71. Hayama, S. et al. Photon-in/photon-out spectroscopy at the I20-scanning beamline at diamond light source. *J. Phys. Condes. Matter* **33**, 11 (2021).
72. Ravel, B. & Newville, M. ATHENA, ARTEMIS, HEPHAESTUS: data analysis for X-ray absorption spectroscopy using IFEFFIT. *J. Synchrotron Radiat.* **12**, 537–541 (2005).
73. Neese, F. The ORCA program system. *Wiley Interdiscip. Rev. -Comput. Mol. Sci.* **2**, 73–78 (2012).
74. Hanwell, M. D. et al. Avogadro: an advanced semantic chemical editor, visualization, and analysis platform. *J. Cheminformatics* **4**, 17 (2012).
75. Najibi, A. & Goerigk, L. The nonlocal kernel in van der waals density functionals as an additive correction: an extensive analysis with special emphasis on the B97M-V and ωB97M-V Approaches. *J. Chem. Theory Comput.* **14**, 5725–5738 (2018).
76. Weigend, F. & Ahlrichs, R. Balanced basis sets of split valence, triple zeta valence and quadruple zeta valence quality for H to Rn: design and assessment of accuracy. *Phys. Chem. Chem. Phys.* **7**, 3297–3305 (2005).
77. Weigend, F. Accurate Coulomb-fitting basis sets for H to Rn. *Phys. Chem. Chem. Phys.* **8**, 1057–1065 (2006).
78. van Lenthe, E., Snijders, J. G. & Baerends, E. J. The zero-order regular approximation for relativistic effects: the effect of spin-orbit coupling in closed shell molecules. *J. Chem. Phys.* **105**, 6505–6516 (1996).
79. Grimme, S., Antony, J., Ehrlich, S. & Krieg, H. A consistent and accurate *ab initio* parametrization of density functional dispersion correction (DFT-D) for the 94 elements H-Pu. *J. Chem. Phys.* **132**, 154104 (2010).
80. Grimme, S., Ehrlich, S. & Goerigk, L. Effect of the damping function in dispersion corrected density functional theory. *J. Comput. Chem.* **32**, 1456–1465 (2011).
81. Towers Tompkins, F. K. et al. Efficient prediction of the local electronic structure of ionic liquids from low-cost calculations. *Phys. Chem. Chem. Phys.* **27**, 8803–8812 (2025).
82. Andersson, K., Malmqvist, P. A., Roos, B. O., Sadlej, A. J. & Wolinski, K. 2nd-order perturbation-theory with a CASSCF reference function. *J. Phys. Chem.* **94**, 5483–5488 (1990).
83. Werner, H. J. & Meyer, W. A quadratically convergent MCSCF method for the simultaneous optimization of several states. *J. Chem. Phys.* **74**, 5794–5801 (1981).
84. Malmqvist, P. A., Pierloot, K., Shahi, A. R. M., Cramer, C. J. & Gagliardi, L. The restricted active space followed by second-order perturbation theory method: theory and application to the study of CuO_2 and Cu_2O_2 systems. *J. Chem. Phys.* **128**, 10 (2008).
85. Finley, J., Malmqvist, P. A., Roos, B. O. & Serrano-Andres, L. The multi-state CASPT2 method. *Chem. Phys. Lett.* **288**, 299–306 (1998).
86. Galván, I. F. et al. OpenMolcas: from source code to insight. *J. Chem. Theory Comput.* **15**, 5925–5964 (2019).
87. Delcey, M. G., Sørensen, L. K., Vacher, M., Couto, R. C. & Lundberg, M. Efficient calculations of a large number of highly excited states for multiconfigurational wavefunctions. *J. Comput. Chem.* **40**, 1789–1799 (2019).
88. Malmqvist, P. A. & Roos, B. O. The CASSCF State Interaction Method. *Chem. Phys. Lett.* **155**, 189–194 (1989).
89. Roos, B. O., Lindh, R., Malmqvist, P., Veryazov, V. & Widmark, P. O. Main group atoms and dimers studied with a new relativistic ANO basis set. *J. Phys. Chem. A* **108**, 2851–2858 (2004).
90. Douglas, M. & Kroll, N. M. Quantum electrodynamical corrections to fine-structure of helium. *Ann. Phys.* **82**, 89–155 (1974).
91. Hess, B. A. Relativistic electronic-structure calculations employing a two-component no-pair formalism with external-field projection operators. *Phys. Rev. A* **33**, 3742–3748 (1986).
92. Hess, B. A., Marian, C. M., Wahlgren, U. & Gropen, O. A mean-field spin-orbit method applicable to correlated wavefunctions. *Chem. Phys. Lett.* **251**, 365–371 (1996).
93. Fouda, A. E. A., Purnell, G. I. & Besley, N. A. Simulation of ultra-fast dynamics effects in resonant inelastic X-ray scattering of gas-phase water. *J. Chem. Theory Comput.* **14**, 2586–2595 (2018).
94. Fouda, A. E. A. et al. Observation of double excitations in the resonant inelastic X-ray scattering of nitric oxide. *J. Phys. Chem. Lett.* **11**, 7476–7482 (2020).
95. Fouda, A. E. A. & Ho, P. J. Site-specific generation of excited state wavepackets with high-intensity attosecond X-rays. *J. Chem. Phys.* **154**, 10 (2021).
96. Delgado-Jaime, M. U. & DeBeer, S. Expedited analysis of DFT outputs: introducing moanalyzer. *J. Comput. Chem.* **33**, 2180–2185 (2012).
97. Lu, T. & Chen, F. W. Multiwfn: a multifunctional wavefunction analyzer. *J. Comput. Chem.* **33**, 580–592 (2012).

Acknowledgements

K.R.J.L. acknowledges support from a Royal Society University Research Fellowship (URF\R\150353 and URF\R\211005) and a Royal Society Research Fellows Enhancement Award (RGF\EA\201064). L.G.P. and F.K.T.T. acknowledge support from a Royal Society Research Fellows Enhanced Research Expenses (RF\ERE\210061). J.M.S. acknowledges support from a Royal Society University Research Fellowship Enhancement Award (RGF\EA\180089). E.G. acknowledges support from a Royal Society Research Grant for Research Fellows (RGF\R1\180053). K.R.J.L. acknowledges support from an EPSRC Capital Award for Early Career Researchers (EP/S017828/1). We acknowledge Diamond Light Source for time on Beamline I20 under Proposals SP24305, SP28565, SP30597, SP33520, and SP36798. A.E.A.F. acknowledges support from the U.S. Department of Energy, Office of Basic Energy Sciences, Division of Chemical Sciences, Geosciences, and Biosciences through Argonne National Laboratory. Argonne is a U.S. Department of Energy laboratory managed by UChicago Argonne, LLC, under contract DE-AC02-06CH11357.

Author contributions

L.G.P. Investigation (Lead—Experiments, ORCA calculations), Formal analysis (Lead), Writing—original draft (Joint), Visualisation (Lead), Project administration (Support). F.K.T.T. Investigation (Support—experiments). J.M.S. Investigation (Support—experiments). N.A. Investigation (Support—experiments). E.G. Investigation (Support—experiments). M.R.D. Formal analysis (Support). S.H. Investigation (Support—experiments), Writing—review & editing (Support). R.P.M. Writing—review & editing (Support), Investigation (Support—ORCA calculations). A.E.A.F. Writing—review & editing (Support), Investigation (Support—MS-RASPT2 calculations). J.D.E. Writing—review & editing (Support), Investigation (Support—ORCA calculations). C.D.S. Conceptualisation (Joint), Supervision (Joint), Investigation (Support), Writing—original draft (Joint), Project administration (Joint). K.R.J.L. Conceptualisation (Joint), Supervision (Joint), Funding acquisition (Lead), Investigation (Support), Writing—original draft (Joint), Resources (Lead), Project administration (Joint).

Competing interests

The authors declare no competing interests.

Additional information

Supplementary information The online version contains supplementary material available at https://doi.org/10.1038/s42004-025-01704-x.

Correspondence and requests for materials should be addressed to Christopher D. Smith or Kevin R. J. Lovelock.

Peer review information *Communications Chemistry* thanks Eva Muchova, Fabian Dankert, and the other anonymous reviewers for their contribution to the peer review of this work.